



Manuel Heimann, Klaus Friedel Ortega and Malte Behrens* **Co₃O₄/BiVO₄ Heterostructures for Photochemical Water Oxidation: The Role of Synthesis Parameters and Preparation Route for the Physico-Chemical Properties and the Catalytic Activity**

<https://doi.org/10.1515/zpch-2019-1477>

Received May 18, 2019; accepted November 19, 2019

Abstract: The synthesis conditions of the semiconductor BiVO₄ have marked influence on its physicochemical and photocatalytic properties. In this work, a pH-controlled co-precipitation route was systematically investigated. Special attention was paid to the pH value during co-precipitation and co-precipitate post-treatment. In a sacrificial photocatalytic water oxidation test, the highest activity was observed for a sample precipitated at pH = 1 and 70 °C, which was post treated at 600 °C in air for 3 h after washing and drying. The activity was further improved by another 90% by the addition of the Co₃O₄-based co-catalyst. Good synergy between semiconductor and co-catalyst was obtained for the deposition of pre-formed nanoparticles at a loading of 0.1 w% (physical impregnation). The effects of different synthesis conditions of the semiconductor and impregnation method for the co-catalyst on the structure, morphology and optical properties of the catalysts were investigated by PXRD, SEM, UV-vis spectroscopy, and TEM, while the water oxidation activity was compared in the dark and with the aid of visible light using cerium (IV) or silver (I) as sacrificial agents, respectively, with the aim of establishing structure-activity correlations. The roles of semiconductor particle anisotropy and co-catalyst particle distribution for optimal photo-activity in the oxygen evolution reaction are discussed.

Keywords: bismuth vanadate; photocatalysis; water oxidation.

***Corresponding author: Malte Behrens**, University of Duisburg-Essen, Faculty of Chemistry and Center for Nanointegration Duisburg-Essen (CENIDE), Universitätsstr. 7, 45141 Essen, Germany, e-mail: malte.behrens@uni-due.de

Manuel Heimann and Klaus Friedel Ortega: University of Duisburg-Essen, Faculty of Chemistry and Center for Nanointegration Duisburg-Essen (CENIDE), Universitätsstr. 7, 45141 Essen, Germany

1 Introduction

Bismuth vanadate, BiVO_4 , is an inorganic yellow pigment. In nature, BiVO_4 may occur as the orthorhombic mineral Pucherite [1, 2], while synthetic BiVO_4 crystallizes in the Scheelite or Zircon structure types as the other two natural minerals Clinobisvanite and Dreyerite, respectively [3–6]. The band gap of monoclinic Scheelite-type BiVO_4 Clinobisvanite is 2.41 eV [3] and this polymorph shows the highest activity in photocatalytic conversions using visible light. In 1998, Kudo et al. showed that BiVO_4 can catalyse the oxidation of water to oxygen using silver nitrate as a sacrificial oxidant [7]. BiVO_4 has been also investigated as photocatalyst for the degradation of organic compounds [8–10], but received most attention as candidate for the anodic half reaction of photoelectrochemical solar water splitting [11–15].

BiVO_4 can be synthesized by several methods like for example solid state reaction of Bi_2O_3 and NH_4VO_3 in air for 5 h at 700–900 °C [7] or decomposition of metalorganic precursors [16]. Solvothermal synthesis has been reported [17, 18], and surfactant-assisted hydrothermal synthesis yields BiVO_4 fibres [19, 20]. Also electrospinning was reported to synthesize active BiVO_4 [21]. Widely applied is the aqueous co-precipitation from an acidic solution of $\text{Bi}(\text{NO}_3)_3$ and NH_4VO_3 using a base as precipitating agent at room temperature [3, 9, 22, 23].

It is well-known that variation of synthesis conditions can affect the physico-chemical properties of (photo)catalysts and their activity quite dramatically. It is important to study these relationships between synthesis, (micro)structural properties and catalytic performance systematically and in detail not only for the purpose of catalyst optimization, but in particular to gain new fundamental insight into catalytic processes from such correlations. In this work, a pH-controlled co-precipitation route for the synthesis of BiVO_4 was investigated. Special attention was paid to the pH value during co-precipitation and the thermal co-precipitate post-treatment either in air (calcination) or under hydrothermal conditions. The effects on the structure, morphology and optical properties of the powder catalysts were investigated and correlated with catalytic activity.

The catalytic performance of semiconductor photocatalysts can be further improved with the aid of suitable co-catalysts [24] that help in enhancing surface redox kinetics and suppressing surface charge recombination [25, 26]. Therefore, 3d transition metal-based co-catalysts have been studied as redox co-catalysts for the oxygen evolution reaction (OER) on BiVO_4 [27–29], among these many cobalt compounds [30–36]. Spinel-type Co_3O_4 has been investigated already since the 1980s as promising electrocatalyst for the OER [37–39]. As a co-catalyst in photochemistry, it was used for example on TiO_2 and CoO_x deposition was found to

improve water oxidation [40]. Cobalt was also used in presence of phosphates in Nocera's famous Co-P₁ catalyst [41], which was also shown to work on BiVO₄ photoanodes [42–44]. Long et al. used Co₃O₄ as co-catalyst for BiVO₄ and deposited it in small amounts (0.8 w%) by impregnation to improve the phenol decomposition under visible light irradiation [45]. Herein, we address the role of the impregnation method to add the co-catalyst and the synergy between light absorber and redox catalyst by comparing the OER in the dark and under visible light irradiation using Ce⁴⁺ and Ag⁺, respectively, as sacrificial agents.

2 Experimental details

2.1 Synthesis

Co-precipitations were conducted in a semi-automatized lab reactor system under controlled conditions (Optimax, Mettler Toledo). The computer-controlled gravimetric dosing and online pH monitoring allowed to keep the pH value nearly constant during the co-precipitation by simultaneous dosing of acidic metal salt solution and the basic precipitating agent. The synthesis of BiVO₄ by precipitating an acidic solution of Bi³⁺ and VO₂⁺ ions with ammonia was conducted at various pH values and 70 °C according to



Bi(NO₃)₃·5 H₂O (Alfa Aesar), NH₄VO₃ (Carl Roth), HNO₃ (Bernd Kraft), ammonia solution (VWR), were used for the co-precipitation. In a typical synthesis, 12.0 g (24 mmol) bismuth nitrate and 2.896 g (24 mmol) ammonium vanadate were dissolved in 400 mL nitric acid (1 mol/L) and dosed into a 1000 mL reactor vessel pre-filled with 150 mL nitric acid (1 mol/L). Three hundred fifty milliliters of the metal solution was added at a constant rate of 2 mL/min. Simultaneously, an appropriate amount of aqueous NH₃ solution (2 mol/L) was added to keep the pH constant at 1, 3 or 9. The reaction mixture was kept at 70 °C. After the dosing was completed (175 min), the co-precipitate was aged in the mother liquor for another 30 min. The yellow solid was filtrated, washed with water, and stored overnight in a drying chamber at 80 °C. Thermal post treatments were done by calcination in a muffle furnace in static air (Nabertherm) in ceramic crucibles containing 700 mg of powder at 400, 600, or 800 °C using a heating rate of 5 °C/min, or by hydrothermal post-treatment. In this case, 1 g of the dried powder was suspended in 120 mL of the mother liquor in a sealed Teflon-lined 250 mL steel autoclave (DAB-3, Berghof Products & Instruments). The treatment was done for 6, 12, or 18 h at 200 °C. The product was re-washed and re-dried as described above.

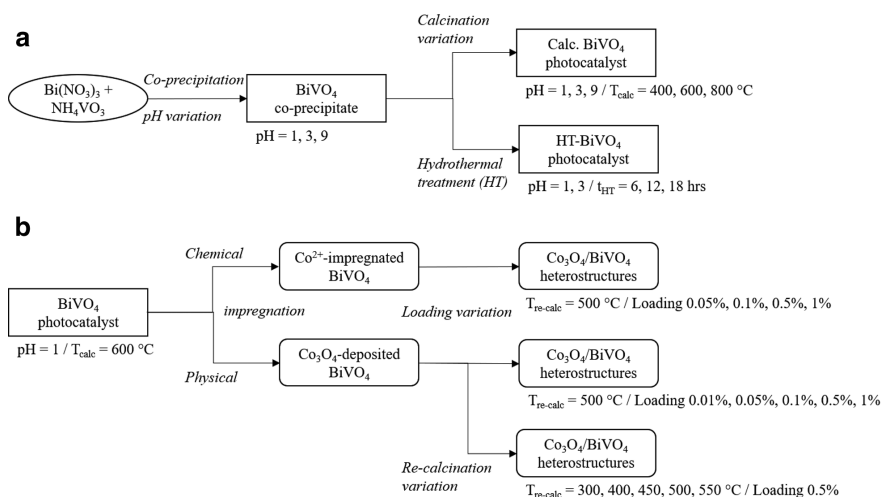
CoO_x was added at co-catalyst following two different approaches, labeled chemical and physical impregnation. For the latter, pre-formed Co_3O_4 nanoparticles were synthesized and deposited on the semi-conducting BiVO_4 . Co_3O_4 was synthesized by simple calcination of commercial cobalt hydroxy carbonate for 3 h according to



The calcination temperatures were adjusted to 300, 400, 500, and 600 °C. To achieve a loading of 0.5 w% Co by the physical impregnation, 6.8 mg (5 mg Co) were dispersed in acetone by ultra-sonication and dropped onto 1000 mg of BiVO_4 (incipient wetness impregnation). The resulting paste was manually agitated and dried at 70 °C for 1 h. Subsequently, the $\text{Co}_3\text{O}_4/\text{BiVO}_4$ heterostructure was re-calcined at various temperatures for 3 h and ground in a mortar.

For the chemical impregnation, an aqueous solution of cobalt nitrate was prepared and the pH was adjusted to 7 using aqueous NH_3 . The concentration was adjusted to yield 5 mg Co in 0.5 mL. These solutions were added to 1000 mg of BiVO_4 as described above to the physical suspension, treated accordingly, and calcined at 500 °C for 3 h.

Scheme 1 gives an overview on the synthesis conditions studied in this work.



Scheme 1: Overview of the different preparation routes and synthesis parameter variations reported in this work for (a) the photocatalyst and (b) the co-catalyst/photocatalyst heterostructure.

2.2 Characterization

X-ray powder diffraction (XRD) was performed on a Bruker D8 Advance diffractometer equipped with a Lynxeye detector using Ni-filtered Cu K α radiation. XRD patterns were recorded with a step size of $0.01^\circ 2\theta$ and a counting time of 0.3 s per step. The samples were dispersed with ethanol on a rotating glass sample holder. The sample porosity and specific surface area were determined by nitrogen physisorption at -196°C in a Nova 3200e (Quantachrome) using 100–3000 mg powder after degassing at 80°C for 2 h in vacuum according to the BET method. Scanning electron microscopy (SEM) images and energy dispersive X-ray spectra (EDX) were obtained in a JSM-6510 SEM (Jeol) equipped with a Quantax 400 EDX detector (Bruker) at a voltage of 5.0 kV and an emission current of 10 μA in vacuum. Transmission electron micrographs (TEM) were recorded in a Cs-aberration corrected Jeol 220FS at 200 kV on Cu grids. The optical band gaps were determined by diffuse reflectance spectroscopy in a Lambda 650 photometer (Perkin Elmer) after background subtraction using the Kubelka-Munk function and Tauc plots. The Zeta potentials and isoelectric points were measured with a Zetasizer Nano ZS (Malvern Instruments) in an aqueous suspension of 10 g/L at pH values between 3 and 10.

2.3 Water oxidation catalysis

Photochemical water oxidation catalysis was performed in a self-made reactor system consisting of a 500 mL stirred vessel for the aqueous suspension of the catalyst, an immersion lamp (150 W Xe with an absorption filter for $\lambda < 340\text{ nm}$, Peshl) and an electrochemical oxygen analyser (EC900, Systech). An Ar carrier gas flow was purged by a mass flow controller through the reactor via a glass frit to achieve fine bubbles and the oxygen content of the gas stream was measured online. The sacrificial agent can be dosed by a dropping funnel. The reactor is shown in Figure 1. The reaction parameters like Ar flow (120 mL/min), filling volume (400 mL), amount of catalyst (1 g/L) and stirring speed (500 rpm) were carefully optimized using commercial WO_3 as photocatalyst [46]. To buffer the formation of protons, 240 mg La_2O_3 (VWR) were added to the reactor. The sacrificial oxidant was 0.815 g (4.8 mmol) of silver nitrate (VWR) in 25 mL water. The measurement time under light irradiation was 120 min. The observed oxygen concentration increases fast as the light is switched on and falls steadily with time. The deposition of reduced metallic silver onto the photocatalyst's surface contributes to this decay, which is why in addition to the cumulative amount of evolved oxygen at 2 h seen in the integral curves, also the initial OER rate was determined from the maximum of the differential curve was evaluated. Error bars

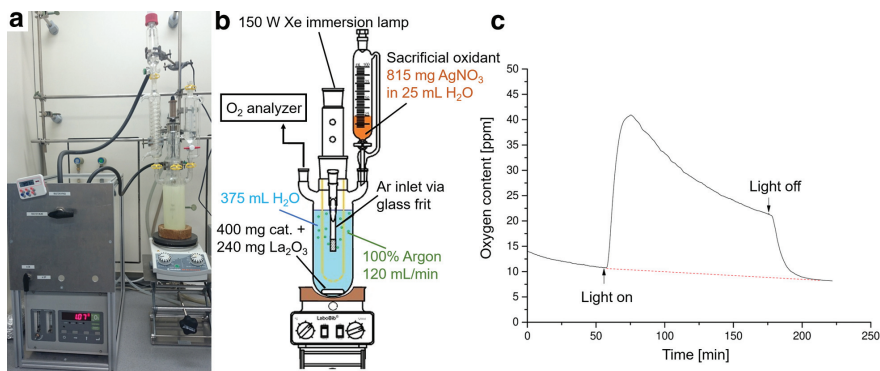


Fig. 1: Photograph (a) and schematic drawing (b) of the setup used for photocatalytic OER in this work. The variation of the oxygen content in the purge gas stream follows the light irradiation (c). For the analysis of photocatalytic activity, either the maximum of the curve was calculated after background subtraction into an initial OER rate, or the period of light irradiation was integrated to compare the amount of evolved oxygen resulting the representation shown in Figures 9 and 11.

for the initial rates and for the amounts of evolved oxygen over 2 h were obtained for selected samples on the basis of two measurements under the same conditions.

In addition to the photocatalytic silver test described above, the OER was also tested in the dark using the cerium ammonium nitrate test (CAN test). Here, cerium (IV) cations act as sacrificial oxidants and allow conclusion on the redox catalytic properties of the co-catalysts in chemical water oxidation. The tests were conducted in a similar, but smaller setup consisting of a 100 mL double-necked flask, which was Ar purged in the same way as for the silver tests. No lamp was used and the CAN solution (12.5 mmol $(\text{NH}_4)_2\text{Ce}(\text{NO}_3)_6$ in 5 mL H_2O) was mixed fast from a dropping funnel into a suspension of 100 mg catalyst and 45 mL H_2O . Gas analysis and kinetic evaluation were done as in the silver test.

3 Results and discussion

3.1 Co-precipitation and post-treatment of BiVO_4

The computer-controlled co-precipitation synthesis of BiVO_4 was conducted as described above at three different pH values 1, 3, and 9. No additive such as TiCl_2 , which was reported as structure-directing agent in the hydrothermal synthesis of BiVO_4 was used [47]. First, the synthesis at $\text{pH} = 1$ is described in detail. The synthesis log in Figure 2a shows that pH and temperature were successfully controlled to be constant over the precipitation and ageing periods. The synthesis was

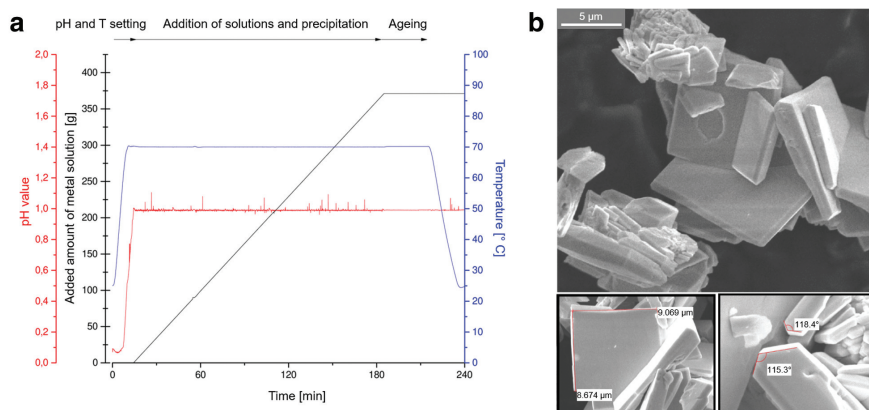


Fig. 2: Synthesis log plot for the computer-controlled constant pH co-precipitation of BiVO_4 at $\text{pH} = 1$ and $T = 70^\circ\text{C}$ (a). SEM micrographs of the resulting BiVO_4 co-precipitate (b).

reproducible and yielded BiVO_4 with platelet-like morphology and an edge length of up to $9\ \mu\text{m}$ as shown in Figure 2b. The specific surface area of the washed and dried sample was low and approximately $1\ \text{m}^2/\text{g}$.

Portions of the sample were calcined at 400 , 600 , and 800°C and tested for photocatalytic OER using silver nitrate at described above. The thermal treatment leads to a marked increase in photocatalytic activity. The sample calcined at 400°C was found to be four times more active than the untreated sample. Calcination at 800°C , however, led to a breakdown of activity back to the level of the pristine BiVO_4 . The direct optical band gap of the most active sample obtained at 600°C was $2.45\ \text{eV}$ – in good agreement with literature [48] – and did not change after calcination at 800°C (Figure 3a). XRD analysis showed only small changes as a function of calcination temperature (Figure 3b).

In all cases, phase-pure monoclinic BiVO_4 was obtained. Close inspection of the line intensity distribution and comparison with the theoretical pattern reveals a preferred orientation effect. The SEM images (Figure 4) confirm the platelet-like morphology of the BiVO_4 crystals, which likely is the origin of this effect. Wang et al. discussed that preferential formation of large (010) facets is beneficial for the photocatalytic activity [47] and introduced the intensity ratio of the peak pair 040 at $30.5^\circ 2\theta$ and 110 near $18.6^\circ 2\theta$ as a measure for this effect, which they found to scale with activity. A large intensity ratio 040/110 indicates stronger preferred orientation. The (010) facets relate to the lateral surfaces of the BiVO_4 platelets and a recent detailed surface science study of this surface has reported by Favaro et al. [49]. Thus, strongly anisotropic particles, i.e. thin platelets, will lead to a large preferred orientation effect in XRD and should be the target of photocatalyst

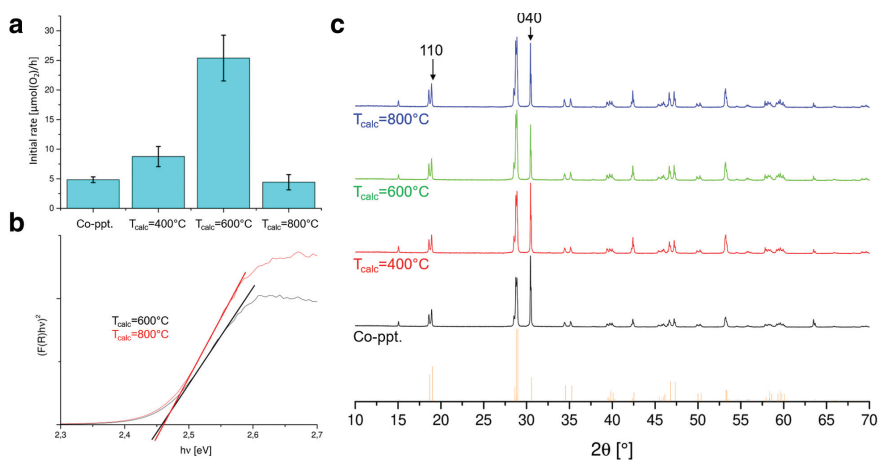


Fig. 3: Initial OER rate determined in the photocatalytic test using silver cations as sacrificial oxidant for the co-precipitate obtained at pH = 1 (co-ppt.) and the catalysts obtained at different calcination temperatures T_{calc} (a). Comparison of the optical band gaps determined for the catalysts calcined at $T_{\text{calc}} = 600$ °C and $T_{\text{calc}} = 800$ °C (b). Powder XRD patterns for the differently calcined photocatalysts in comparison with literature data for BiVO₄ (PDF 01-083-1699). The 110 and 040 peaks are marked (c).

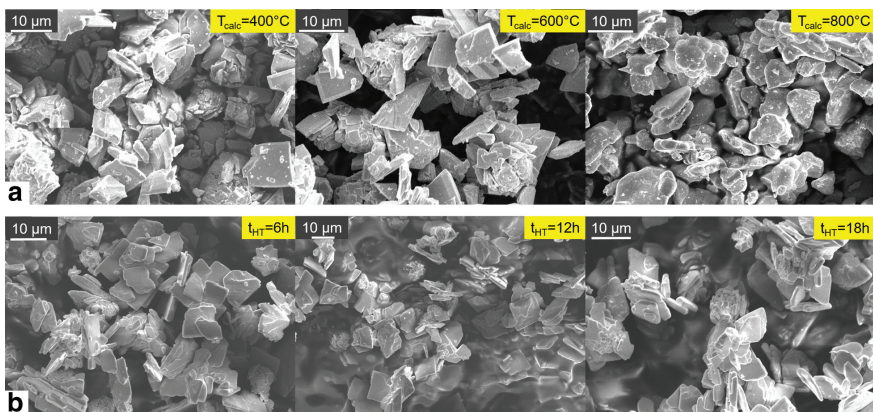


Fig. 4: Comparison of the SEM images obtained for the materials resulting from the co-precipitated shown in Figure 2b after different post-treatments under variation of the calcination temperature T_{calc} (a) or the duration of hydrothermal post-treatment t_{HT} in the mother liquor (b).

synthesis. As an explanation for this assumption, the anisotropic platelet form of BiVO₄ was reported to contribute to the effectiveness of charge separation. According to the DFT calculations of Li et al. [50], a shift between the electronic energy

levels at (010) and (110) surfaces leads to an electron flow from the latter to the former. A preferred orientation in the diffractograms is observed after all calcination temperatures, but clearly lowered at temperatures of 600 °C and 800 °C. The SEM investigation shows that the sharp edges of the crystallites withstand the calcination at 400 and 600 °C. Some smaller segregated particles appear as bright spots in the micrographs and can be observed on the surface of the larger BiVO_4 crystals, otherwise the material remains relatively unchanged (Figure 4a). Only after calcination at 800 °C, a more pronounced change is observed and the BiVO_4 crystals lose their sharp edges and well-defined crystal facets indicating the beginning of thermal degradation (sintering) into more roundish shaped particles. This is probably related to the beginning thermal decomposition towards oxygen-rich composition such as $\text{Bi}_2\text{VO}_{5.5}$ [51] and likely is the explanation for the reduced photo-catalytic activity, which was observed to depend on high crystallinity to favor charge mobility and hinder recombination at defect sites [52].

Thus, it can be hypothesized that the calcination has at least two (counter-) effects. Thermal annealing leads to the segregation of material that was trapped in the bulk of the co-precipitate to the surface, which likely is associated with a favorable re-crystallization of the bulk. This may be a positive effect for photocatalysis due to the higher crystallinity of the bulk semiconductor. A similar positive effect of annealing was recently also reported for the photoelectrochemical properties of BiVO_4 [53]. On the other hand, too high temperature lead to sintering of the anisotropic crystals into less-defined shapes as observed at 800 °C. Furthermore, loss of vanadium may occur from BiVO_4 calcined in air at temperatures above 450 °C leading to detrimental point defects in the lattice as described recently by Lamers et al. [54], who interestingly also observed a positive effect of milder calcination. With both loss of anisotropy and vanadium, also the photocatalytic activity degrades and calcination at 600 °C represent the best compromise between the two effects in our sample series. Such detrimental effect of post-calcination was also reported by Kho et al. for flame-made BiVO_4 [55], which is why the authors successfully used a milder aqueous route for BiVO_4 post-treatment.

This model for the effect of thermal post-treatment was thus also further tested for isothermic hydrothermal conditions. Here, the co-precipitate was suspended in the mother liquor (pH = 1) and instead of the temperature the treatment time was varied. To avoid the negative sintering effect at too high temperatures, heating was set to 200 °C for 6, 12 and 18 h. Again, the photocatalytic activity was markedly increased by a factor of three for the sample treated for 18 h (Figure 5a). However, it needs to be noted that the difference between 6 and 12 h was only small and that the size of the activity promotion after 18 h was not well reproducible. Opposed to the dry calcination series, XRD revealed that the preferred orientation effect was increased after 18 h of hydrothermal treatment,

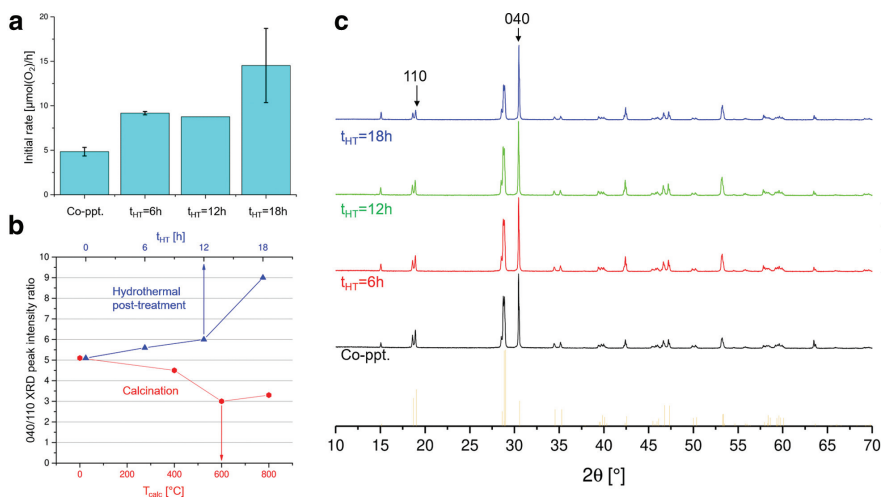


Fig. 5: Initial OER rate determined in the photocatalytic test using silver cations as sacrificial oxidant for the co-precipitate obtained at $\text{pH} = 1$ (co-ppt.) and the catalysts obtained at different durations of hydrothermal post-treatment t_{HT} (a). Comparison of the evolution of the intensity ratio for the 040 and 110 peaks that indicate the crystallite anisotropy (see text for details) for the two different post-treatments (b). Powder XRD patterns for the different hydrothermally treated photocatalysts in comparison with literature data for BiVO_4 (c).

which, if related to crystal anisotropy, may be the reason for the increased activity (Figure 5c). SEM images show that the general crystal shape with sharp edges remained similar independent of the reaction time indicating that the increased preferred orientation after 18 h may rather be caused by the de-agglomeration of the crystals than by changes in shape. Also the surface cleanliness was not affected by the hydrothermal treatment (Figure 4b), but possible segregations may have dissolved in the liquid.

In an attempt to establish the preferred orientation effect as indicator for the structural changes, the 040/110 intensity ratio change was determined and plotted as a function of post-treatment conditions, calcination temperature and duration of hydrothermal treatment, respectively, in Figure 5b. It is noted that the ratio should be <1 for a statistical orientation distribution. The observed values between 3 and 9 indicate preferred orientation due to anisotropic crystallites for all samples, which arises from a preferred stacking in the powder layer upon sample preparation on the holder with the lateral dimensions of the flat crystals being perpendicular to the scattering vector with increased probability. In this situation, the relative extent of preferred orientation can only be safely related to crystal anisotropy if effects of agglomeration are absent. It can be seen that the effect on preferred orientation was different for calcination and hydrothermal treatment.

It was lowered for the former and increased for the latter. For the hydrothermally treated sample series, an apparent correlation with the photocatalytic activity was observed. However, since the activity was increased also in case of the calcined samples, it is clear that the crystal anisotropy determined from the extent of preferred orientation in powder XRD under neglect of agglomeration effects is not the only structural factor influencing photocatalysis. Another effect, likely related to thermal annealing and re-crystallization, must over-compensate this factor in case of the most active sample calcined at 600 °C. Such re-crystallization may be related to the reversible phase change from monoclinic to tetragonal Scheelite structure of BiVO_4 expected at 255 °C [2, 3], which occurred during calcination, but not in the hydrothermal experiments.

If BiVO_4 was synthesized at $\text{pH} = 3$, an amorphous product was isolated with a specific surface area of $1 \text{ m}^2/\text{g}$. This co-precipitate was subjected to the same thermal treatments as described above for the sample obtained at $\text{pH} = 1$. In all cases, monoclinic BiVO_4 crystallized (Figure 6b). The preferred orientation effect is by no means as prominent as observed for the samples obtained as $\text{pH} 1$ suggesting a rather statistic distribution of the crystal's orientation. After calcination at 400 °C and 600 °C, the splittings of the 110/011 and 12-1/121 double peaks just below 20 and 30° 2θ , respectively, are only weakly pronounced. This observation could be explained by a partial stabilization of the tetragonal Scheelite structure of BiVO_4 even after cooling back to room temperature. Interestingly, despite the completely amorphous structure, the photocatalytic activity of the co-precipitate was similar (initial rate 5.7 $\mu\text{mol}/\text{h}$) as observed for the crystalline product obtained at $\text{pH} = 1$ (4.9 $\mu\text{mol}/\text{h}$). Again, a further increase was observed for the calcined samples and this increase continued even after calcination at 800 °C unlike the sample series at $\text{pH} = 1$ (Figure 6a). The SEM micrographs offer an explanation for this observation as the evolution to larger and more anisotropic crystals can be seen (Figure 6b). Thus, higher crystallinity and a favorable crystal shape develop during calcination of the material at $\text{pH} = 3$, while these properties tend to vanish at high temperature for the co-precipitate obtained at $\text{pH} = 1$. The hydrothermally treated samples show the highest activity for the shorted treatment time of 6 h with a decay at 12 h and a stabilization for 18 h. The particle aggregates do not change substantially upon hydrothermal treatment in SEM (not shown). It is noted that the reproducibility of the catalytic activity was lower for catalysts synthesized at $\text{pH} = 3$ than $\text{pH} = 1$ as indicated by the error bars in Figure 6a.

If BiVO_4 was synthesized at $\text{pH} = 9$, again an amorphous co-precipitate was obtained. Upon calcination at 400 °C, crystallization of BiVO_4 was observed, while $\text{Bi}_2\text{VO}_{5.5}$ was obtained at 800 °C (Figure 7b). The calcination was accompanied by an intensification of the color (Figure 7a) that is also observed

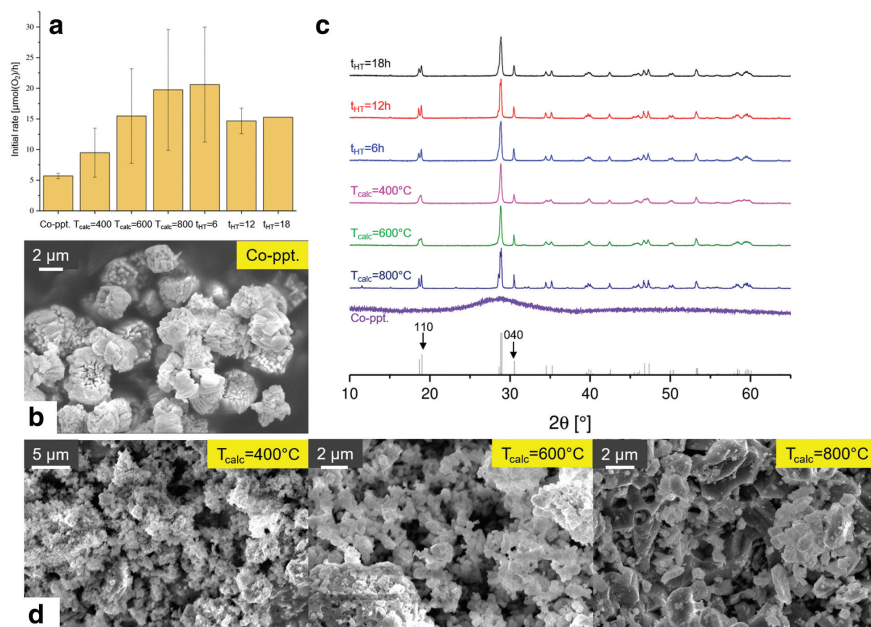


Fig. 6: Initial OER rate determined in the photocatalytic test using silver cations as sacrificial oxidant for the co-precipitate obtained at pH = 3 (co-ppt.) and the catalysts obtained by calcination at different temperatures T_{calc} or at different durations of hydrothermal post-treatment t_{HT} (a). SEM image of the co-precipitate at pH = 3 (b). Powder XRD patterns for the differently post-treated photocatalysts in comparison with literature data for BiVO_4 (c). Evolution of the microstructure studied by SEM for the sample series obtained at different T_{calc} (d).

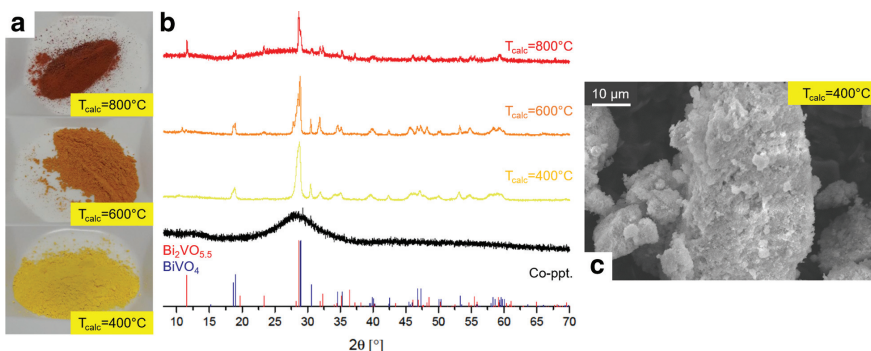


Fig. 7: Photographs of the powders obtained by calcination of the co-precipitate obtained at pH = 9 (co-ppt.) at different calcination temperatures T_{calc} (a) and the corresponding powder XRD patterns in comparison with literature data for BiVO_4 (PDF 01-083-1699) and $\text{Bi}_2\text{VO}_{5.5}$ (PDF 81-221) (b). SEM image of the sample calcined at $T_{\text{calc}} = 400^\circ\text{C}$ (c).

in the evolution of the optical band gaps from 2.8 eV (co-precipitate), over 2.5 eV (400 °C) and 2.3 eV (600 °C) to finally 1.8 eV at 800 °C. Despite the presence of monoclinic BiVO_4 and a suitable band gap after calcination at 400 °C, no photocatalytic activity was observed for any of the sample synthesized at pH = 9. For this aforementioned catalyst, this may be due to the isotropic particle shape as seen in the SEM image (Figure 7c) and by the low 040/110 intensity ratio of only 1.5. Thus, the morphology is clearly different and less favorable for photocatalysis compared to the active BiVO_4 photocatalysts synthesized at lower pH.

3.2 Co_3O_4 co-catalyst deposition on BiVO_4

The most active photocatalyst of the sample described in section 3.1 was the BiVO_4 catalyst synthesized at pH = 1 and calcined at 600 °C for 3 h with an initial OER rate of 25 $\mu\text{mol/h}$ in our test. This photocatalyst was used for the co-catalyst deposition experiments to obtain $\text{Co}_3\text{O}_4/\text{BiVO}_4$ heterostructures. The deposition of Co_3O_4 was done using two different impregnation procedures, physical impregnation of pre-formed particles and chemical impregnation of dissolved Co (II) precursors.

For the physical impregnation, Co_3O_4 was synthesized from commercial cobalt hydroxy carbonate $\text{Co}_2\text{CO}_3(\text{OH})_2$ by calcination in air. The Co_3O_4 spinel is the stable product 270 °C (onset of decomposition according to thermogravimetric analysis, not shown) and 900 °C, where thermal reduction to CoO occurs. The thermal decomposition synthesis was done at 400, 500, and 600 °C. XRD confirms the presence of Co_3O_4 in all cases with a pronounced narrowing of the peaks with increasing temperature indicating crystallite growth (Figure 8a). Using the Scherrer equation, the average crystallite sizes were determined to be around 15 nm at 300 °C with a steady increase to 35 nm at 900 °C (Figure 8b). It is noted that the product calcined at the lowest temperature of 300 °C exhibits an inhomogeneous microstructure according to SEM with small isotropic particles on the nm scale on the one and larger platelet-like particles with lateral dimensions on the μm scale (Figure 8c). With increasing calcination temperature, more of the platelets are observed. This may be the reason why the specific surface area was found not to decrease steadily but increased from 30 m^2/g at 300 °C to a maximum of 34 m^2/g at 400 °C before a steady decrease to 12 m^2/g was observed (Figure 8b). The redox catalytic activity of the co-catalyst was evaluated in the dark using the CAN test. Highest activity was found for the catalyst calcined at 300 °C (Figure 8b). The activity was close to that obtained at 400 °C, but higher calcination temperature led to a steady decrease in activity proportional to the exposed surface area of the catalyst. To test for the effect of the microstructural inhomogeneity of the catalyst obtained at 300 °C, the sample was pressed through

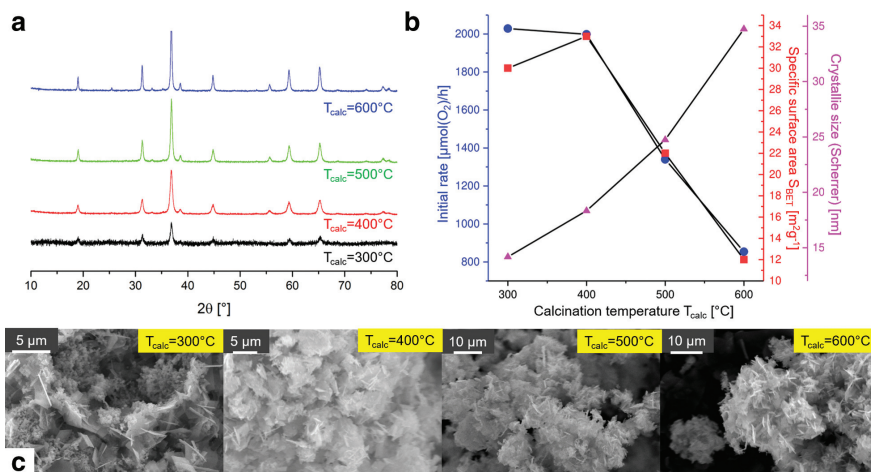


Fig. 8: Powder XRD patterns of the redox catalysts obtained by thermal decomposition of cobalt hydroxy carbonate at different calcination temperatures T_{calc} (a). The patterns correspond to spinel-type Co_3O_4 . Evolution of initial OER rate determined in the dark using cerium (IV) cations as sacrificial oxidant (CAN test), of the specific surface area S_{BET} and of the crystallite size determined from the XRD patterns in (a) using the Scherrer equation (b). SEM images of the calcination products obtained at different calcination temperatures T_{calc} (c).

a syringe filter with 450 nm pores to separate the larger platelets from the smaller isotropic particles. This sieved sample showed approximately the same activity as the pristine one suggesting that the microstructure of the Co_3O_4 does not play a decisive role for the chemical water oxidation catalysis in the dark.

The Co_3O_4 co-catalyst after calcination at 300 °C was used for the physical impregnation experiments as described in the experimental section. After drying the resulting 0.5 w% $\text{Co}_3\text{O}_4/\text{BiVO}_4$ heterostructures, they were subjected to re-calcination. The presence of the co-catalyst as well as calcination led to a marked increase in the photocatalytic activity (Figure 9a). The increase with temperature was highest at 500 °C. A possible explanation is that the calcination triggers chemical interaction between the two phases leading to a higher contact areas and thus easier charge carrier transport between semiconductor and co-catalyst. A similar positive annealing effect was reported for the contact area between BiVO_4 and an FTO back contact by Yan et al. [56]. 500 °C was used as optimal calcination temperature for the loading variation study. The loading was varied from 0.01 to 1 w% and 0.1 w% was found to deliver the best catalytic performance (Figure 9b). The amount of produced oxygen after 2 h was 18.15 μmol and thus 90% higher compared to the bare BiVO_4 without co-catalyst (9.5 μmol). The activity first increased with co-catalyst loading and then decayed again for too

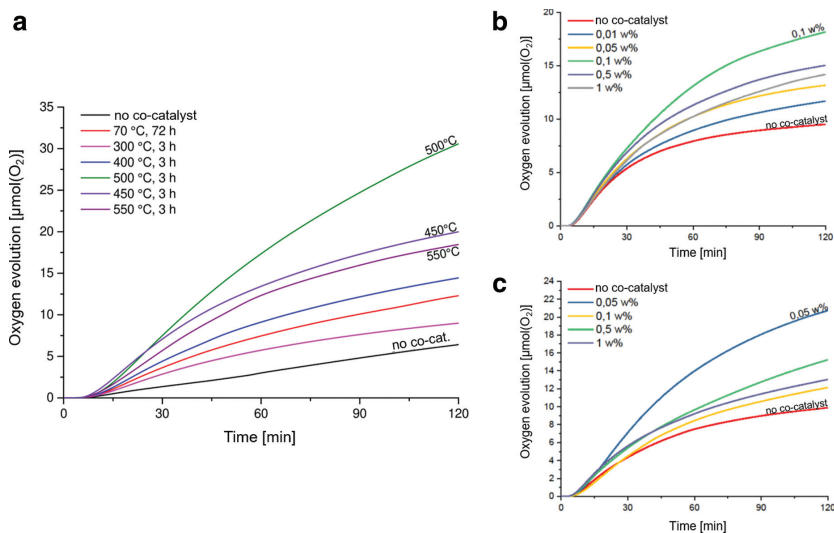


Fig. 9: Evolved oxygen with time in the photocatalytic test using silver cations as sacrificial oxidant for the $\text{Co}_3\text{O}_4/\text{BiVO}_4$ heterostructure photocatalysts (0.5 w% Co) obtained by physical impregnation and post-treatment at different calcination temperatures and times (a). Comparison for different Co loadings and $T_{\text{calc}} = 500\text{ }^\circ\text{C}$ (b). Comparison for the catalysts obtained by chemical impregnation at different loadings at $T_{\text{calc}} = 500\text{ }^\circ\text{C}$ (c). Note that this Figure displays only one run for each catalyst for the sake of clarity. In selected cases, two runs have been performed to determine error bars as described in the experimental section.

high loadings of 0.5 and 1 w%. This behavior has been often observed and is typically reasoned by the interfering of the dark co-catalyst with light absorption at too high loading, although no substantial color change could be observed with the bare eye for the samples investigated here. TEM images show that the Co_3O_4 co-catalyst was distributed on the surface of the semiconductor in form of nanoparticles with a size around 20–50 nm at a loading of 0.5 w% (Figure 10a). The particle loading is far from a full coverage and TEM-EDX mapping in Figure 10a confirms that the observed surface decoration of BiVO_4 is indeed due to cobalt oxide. The interface contact between semiconductor and co-catalyst seems intimate in the high-resolution images and the particles are aggregated to a low extent with only a few primary particles residing on the same spot of the semiconductor surface. These beneficial properties likely are the reason for the high catalytic activity of the heterostructured catalyst.

In the SEM images, the Co_3O_4 particles appear as bright spots (Figure 10a, see arrows in the last panel). The high dispersion is confirmed with better statistics than in TEM, but it can be seen that the distribution is not fully homogeneous and some parts of the semiconductor surface are more covered than others. However,

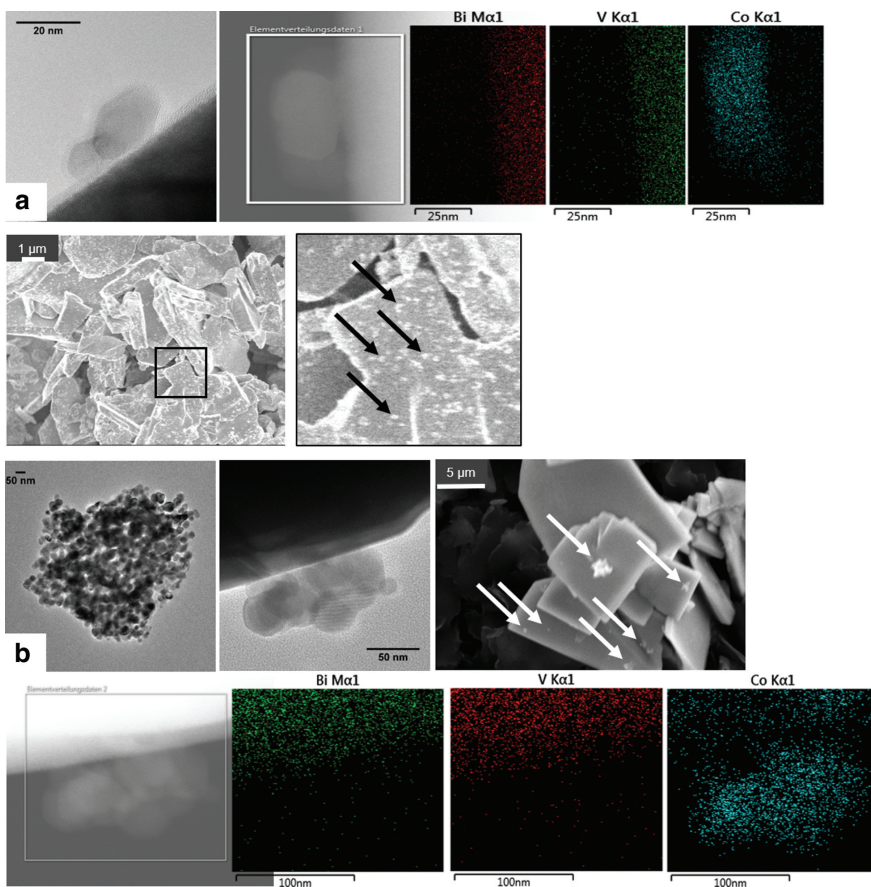


Fig. 10: Electron microscopy (TEM, TEM-EDX mapping and SEM) images for the $\text{Co}_3\text{O}_4/\text{BiVO}_4$ heterostructure photocatalysts (0.5 w% Co) obtained by physical (a) and chemical (b) impregnation.

no clear evidence for a preferred deposition on the 011 and 110 faces that typically are found at the edge planes of the BiVO_4 platelets can be confirmed for the method of physical impregnation investigated here. These faces and not the lateral surface of the large BiVO_4 platelets are assumed to be responsible for the OER half reaction because the holes tend to accumulate there as reported by Li et al. [50]. It was shown that by using the method of photodeposition, it was possible to address the lateral and the edge planes of the BiVO_4 separately with different co-catalyst.

Chemical impregnation with cobalt nitrate was tested as an alternative route to deposit the Co_3O_4 co-catalyst. The isoelectric point of the BiVO_4 was determined from the pH dependence of the Zeta potential and found to be at $\text{pH} = 4.5$. The impregnation was performed at $\text{pH} = 7$ to utilize attractive electrostatic interaction between the negatively charged surface of BiVO_4 and the cobalt cations in solution. Based on the previous results, the samples were calcined at 500°C to transform the deposited cobalt precursor into Co_3O_4 and to increase the interaction between the two components. The loading variation study revealed a lower optimal co-catalyst loading for chemical impregnation, which was only 0.05 w% (Figure 9c). This loading led to evolution of $25.8 (\pm 5.1)$ μmol oxygen after 2 h, comparable with the best catalyst obtained by physical impregnation. While this low amount of Co_3O_4 could not be captured analytically in a reliable manner, the 0.5 w% loaded catalyst was investigated by electron microscopy and showed some Co_3O_4 aggregates in TEM (Figure 10b). Some of these aggregates were even completely released from the semiconductor surface (Figure 10b, first panel). Deposits at the surface were larger than those obtained by physical impregnation and consisted of several primary particles, where only those closest to the surface showed clear primary interaction to the semiconductor. TEM-EDX confirms cobalt oxide. A low number of relatively large aggregates can also be seen in the SEM images (Figure 10b, see arrows in the last panel). The likelihood that the co-catalyst particles cover the edge facets of the semiconductor platelets, which are assumed to be active for OER is low. This unfavorable Co_3O_4 distribution may serve as a likely explanation for the only moderate co-catalysis due to hindered charge carrier transport between semiconductor and redox catalyst at this loading.

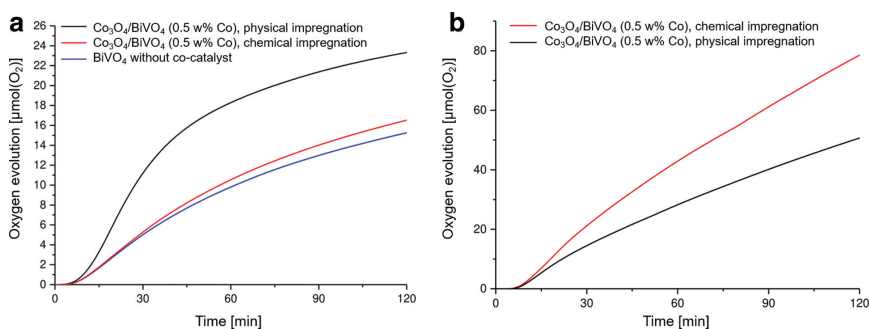


Fig. 11: Evolved oxygen with time of the two samples shown in Figure 10, $\text{Co}_3\text{O}_4/\text{BiVO}_4$ heterostructure photocatalysts (0.5 w% Co) obtained by physical and chemical impregnation, in the photochemical OER (silver test) in comparison with the bare semiconductor (a) and in the chemical OER (CAN test) in the dark (b).

In a comparison of the two deposition routes for the same Co loading of 0.5 w%, the photocatalytic tests showed the results that was expected when considering the TEM images. The physically impregnated catalyst shows a higher performance. The chemical impregnation leads to a catalyst with a similar initial rate like the bare BiVO_4 , while only at longer reaction time a slightly higher oxygen evolution was observed (Figure 11a). Interestingly, when the two heterostructures were compared in the chemical water oxidation in the dark (CAN test), the chemically impregnated sample outperformed the physically impregnated one (Figure 11b), while the bare BiVO_4 was completely inactive (not shown). The better activity might be explained by a higher specific cobalt oxide surface area in the porous aggregates after physical impregnation compared to the less exposed particles with stronger interaction to the semiconductor surface obtained after physical interaction. However, the results clearly show that the high redox activity of the chemically impregnated co-catalyst cannot be utilized in photocatalysis as a result of the unfavorable microstructure of the heterostructured catalyst.

4 Conclusion

It was shown that constant pH co-precipitation is an attractive way to synthesize BiVO_4 photocatalyst and that pH has marked influence on the activity in the OER. Active samples were obtained at pH = 1 and 3, while the co-precipitate obtained at pH = 9 was complexly inactive. Interestingly, at pH = 3, photocatalytic activity was detected despite the absence of crystallinity. In addition to pH, also thermal post-treatment processes were found to affect photocatalysis. Calcination in air as well as hydrothermal treatment in the mother liquor can improve the catalytic properties. This may be explained with an increase in morphological anisotropy for the hydrothermal treatment and with defect annealing during calcination. Addition of Co_3O_4 as co-catalyst further improves the OER activity of the resulting heterostructure. The promotion was strongest for low loadings of 0.05–0.1 w% and re-calcination at 500 °C. The distribution of the co-catalyst particles on the semiconductor is an important factor to enable easy transfer of charge carriers between BiVO_4 and Co_3O_4 . The deposition by physical impregnation of pre-formed nanoparticles was effective for this purpose.

Acknowledgments: This work was supported by the Deutsche Forschungsgemeinschaft (DFG) within the Priority Program SPP 1613 “Fuels Produced Regeneratively Through Light-Driven Water Splitting: Clarification of the Elemental Processes Involved and Prospects for Implementation in Technological Concepts” (BE4767/2-2). The fruitful discussions and the collaborative spirit in the SPP are greatly acknowledged. We thank DFG core facility “Interdisciplinary Center for

Analytics on the Nanoscale (ICAN)” at the University of Duisburg-Essen and Prof. S. Schulz and Prof. M. Epple of the University Duisburg-Essen for allocating access to their characterization facilities. We thank Dr. Markus Heidelmann (ICAN) for the TEM measurements and for fruitful discussions. Toni Kropf, Tim Kox, and André Borutta are gratefully acknowledged for their contributions to this work during their chemistry studies at the University of Duisburg-Essen.

References

1. A. W. Sleight, H.-Y. Chen, A. Ferretti, D. E. Cox, *Mater. Res. Bull.* **14** (1979) 1571.
2. D. Zhou, L.-X. Pang, D.-W. Wang, I. M. Reaney, *J. Mater. Chem. C* **6** (2018) 9290.
3. S. Tokunaga, H. Kato, A. Kudo, *Chem. Mater.* **13** (2001) 4624.
4. Y. Park, K. J. McDonald, K.-S. Choi, *Chem. Soc. Rev.* **42** (2013) 2321.
5. G. Dreyer, E. Tillmanns, *Neues Jahrb. Mineral. Monatsh.* (1981) 151.
6. D. Trung Tri Trinh, W. Khanitchaidecha, D. Channei, A. Nakaruk, *Res Chem Intermed.* **45** (2019) 5217.
7. A. Kudo, K. Ueda, H. Kato, I. Mikami, *Catal. Lett.* **53** (1998) 299.
8. S. Kohtani, M. Koshiko, A. Kudo, K. Tokumura, Y. Ishigaki, A. Toriba, *Appl. Catal. B* **43** (2003) 573.
9. S. Kohtani, S. Makino, A. Kudo, K. Tokumura, Y. Ishigaki, T. Matsunaga, O. Nikaido, K. Hayakawa, R. Nakagaki, *Chem. Lett.* **31** (2002) 660.
10. H. Xu, H. Li, C. Wu, J. Chu, Y. Yan, H. Shu, *Mater. Sci. Eng. B* **147** (2008) 52.
11. Z. Wang, X. Huang, X. Wang, *Catal. Today* **335** (2019) 31.
12. F. M. Toma, J. K. Cooper, V. Kunzelmann, M. T. McDowell, J. Yu, D. M. Larson, N. J. Borys, C. Abelyan, J. W. Beeman, K. M. Yu, J. Yang, L. Chen, M. R. Shaner, J. Spurgeon, F. A. Houle, K. A. Persson, I. D. Sharp, *Nat. Commun.* **7** (2016) 12012.
13. Z.-F. Huang, L. Pan, J.-J. Zou, X. Zhang, L. Wang, *Nanoscale* **6** (2014) 14044.
14. Y. Park, K. J. McDonald, K.-S. Choi, *Chem. Soc. Rev.* **42** (2013) 2321.
15. F. F. Abdi, L. Han, A. H. M. Smets, M. Zeman, B. Dam, R. van de Krol, *Nat. Commun.* **4** (2013) 3195.
16. K. Sayama, A. Nomura, Z. G. Zou, R. Abe, Y. Abe, H. Arakawa, *Chem. Commun.* (2003) 2908.
17. Y. Zhou, K. Vuille, A. Heel, B. Probst, R. Kontic, G. R. Patzke, *Appl. Catal. A* **375** (2010) 140.
18. T.-G. Vo, J.-M. Chiu, C.-Y. Chiang, Y. Tai, *Solar Energy Mater. Solar Cells* **166** (2017) 212.
19. L. Zhang, D. R. Chen, X. L. Jiao, *J. Phys. Chem. B* **110** (2006) 2668.
20. J. Q. Yu, A. Kudo, *Chem. Lett.* **34** (2005) 850.
21. M. Yu, C. Shang, G. Ma, Q. Meng, Z. Chen, M. Jin, L. Shui, Y. Zhang, Z. Zhang, M. Yuan, X. Wang, G. Zhou, *Appl. Surf. Sci.* **481** (2019) 255.
22. S. Kohtani, J. Hiro, N. Yamamoto, A. Kudo, K. Tokumura, R. Nakagaki, *Catal. Commun.* **6** (2005) 185.
23. C. Ravidhas, J. A. Juliat, P. Sudhagar, A. Devadoss, C. Terashima, K. Nakata, A. Fujishima, A. Moses Ezhil Raj, C. Sanjeeviraja, *Mater. Sci. Semicond. Proc.* **30** (2015) 343.
24. J. Yang, D. Wang, H. Han, C. Li, *Acc. Chem. Res.* **46** (2013) 1900.
25. C. Zachäus, F. F. Abdi, L. M. Peter, R. van de Krol, *Chem. Sci.* **8** (2017) 3712.
26. F. A. L. Laskowski, M. R. Nellist, J. Qiu, S. W. Boettcher, *J. Am. Chem. Soc.* **141** (2019) 1394.
27. Q. Huang, Y. Qiu, H. Luo, Y. Yuan, X. Li, Z. Wang, W. Mai, *Mater. Lett.* **249** (2019) 128.

28. J. A. Seabold, K.-S. Choi, *J. Am. Chem. Soc.* **134** (2012) 2186.
29. L. Gao, F. Li, H. Hu, X. Long, N. Xu, Y. Hu, S. Wei, C. Wang, J. Ma, J. Jin, *ChemSusChem* **11** (2018) 2502.
30. H. A. E. Hagelin-Weaver, G. B. Hoflund, D. M. Minahan, G. N. Salaita, *Appl. Surf. Sci.* **235** (2004) 420.
31. K. Trzciński, M. Szkoda, K. Szulc, M. Sawczak, A. Lisowska-Oleksiak, *Electrochim. Acta* **295** (2019) 410.
32. T.-G. Vo, Y. Tai, C.-Y. Chiang, *J. Catal.* **370** (2019) 1.
33. S. Wang, T. He, J.-H. Yun, Y. Hu, M. Xiao, A. Du, L. Wang, *Adv. Funct. Mater.* **28** (2018) 1802685.
34. J. H. Kim, S. Han, Y. H. Jo, Y. Bak, J. S. Lee, *J. Mater. Chem. A* **6** (2018) 1266.
35. T. Palaniselvam, L. Shi, G. Mettela, D. H. Anjum, R. Li, K. P. Katuri, P. E. Saikaly, P. Wang, *Adv. Mater. Interf.* **4** (2017) 1700540.
36. M. F. Lichterman, M. R. Shaner, S. G. Handler, B. S. Brunschwig, H. B. Gray, N. S. Lewis, J. M. Spurgeon, *J. Phys. Chem. Lett.* **4** (2013) 4188.
37. C. Iwakura, A. Honji, H. Tamura, *Electrochim. Acta* **26** (1981) 1319.
38. P. Rasiyah, A. C. C. Tseung, *J. Electrochem. Soc.* **130** (1983) 365.
39. L. Han, S. Dong, E. Wang, *Adv. Mater.* **28** (2016) 9266.
40. Y. Q. Wu, G. X. Lu, S. Li, Y. Wu, G. Lu, S. Li, *J. Photochem. Photobiol. A* **181** (2006) 263.
41. M. W. Kanan, D. G. Nocera, *Science* **321** (2008) 1072.
42. C. Liu, H. Luo, Y. Xu, W. Wang, Q. Liang, N. Mitsuzaki, Z. Chen, *J. Mater. Sci.* **54** (2019) 10670.
43. S. K. Pilli, T. E. Furtak, L. D. Brown, T. G. Deutsch, J. A. Turner, A. M. Herring, *Ener. Env. Sci.* **4** (2011) 5028.
44. F. F. Abdi, N. Firet, A. Dabirian, R. van de Krol, *Mater. Res. Soc. Symp. Proc.* **1446** (2012) 7.
45. M. C. Long, W. M. Cai, J. Cai, B. X. Zhou, X. Y. Chai, Y. H. Wu, *J. Phys. Chem. B* **110** (2006) 20211.
46. M. Heimann, *Synthese und Charakterisierung von co-Katalysator/Photohalbleiter-Kompositen für die photokatalytische Wasserspaltung*, Dissertation, Faculty of Chemistry, University of Duisburg-Essen (2017).
47. D. Wang, H. Jiang, X. Zong, Q. Xu, Y. Ma, G. Li, C. Li, *Chem. Eur. J.* **17** (2011) 1275.
48. A. Walsh, Y. Yan, M. N. Huda, M. M. Al-Jassim, S.-H. Wie, *Chem. Mater.* **21** (2009) 547.
49. M. Favaro, R. Uecker, S. Nappini, I. Piš, E. Magnano, H. Bluhm, R. van de Krol, D. E. Starr, *J. Phys. Chem. C* **123** (2019) 8347.
50. R. Li, F. Zhang, D. Wang, J. Yang, M. Li, J. Zhu, X. Zhou, H. Han, C. Li, *Nat. Commun.* **4** (2013), 1432.
51. M. Touboul, C. Vachon, *Thermochim. Acta* **133** (1988) 61.
52. A. Kudo, Y. Miseki, *Chem. Soc. Rev.* **38** (2009) 253.
53. L. Shi, S. Zhuo, M. Abulikemu, G. Mettela, T. Palaniselvam, S. Rasul, B. Tang, B. Yan, N. B. Saleh, P. Wang, *RSC Adv.* **8** (2018) 29179.
54. M. Lamers, S. Fiechter, D. Friedrich, F. F. Abdi, R. van de Krol, *J. Mater. Chem. A* **6** (2018) 18694.
55. Y. K. Kho, W. Y. Teoh, A. Iwase, L. Mädler, A. Kudo, R. Amal, *ACS Appl. Mater. Interf.* **3** (2011) 1997.
56. D. Yan, X. Fu, Z. Shang, J. Liu, H. Luo, *Chem. Eng. J.* **361** (2019) 853.

DuEPublico

Duisburg-Essen Publications online

UNIVERSITÄT
DUISBURG
ESSEN

Offen im Denken

ub | universitäts
bibliothek

This text is made available via DuEPublico, the institutional repository of the University of Duisburg-Essen. This version may eventually differ from another version distributed by a commercial publisher.

DOI: 10.1515/zpch-2019-1477

URN: urn:nbn:de:hbz:464-20210303-171351-6



This work may be used under a Creative Commons Attribution 4.0 License (CC BY 4.0).